

# A COUPLED RELUCTANCE NETWORK APPROACH TO SELF-SENSING

**Eugén O. Ranft**

Dept. of Electrical Eng., North-West Univ., Potchefstroom, 2531 South Africa  
[Eugen.Ranft@nwu.ac.za](mailto:Eugen.Ranft@nwu.ac.za)

**George van Schoor**

Dept. of Electrical Eng., North-West Univ., Potchefstroom, 2531 South Africa  
[George.vanSchoor@nwu.ac.za](mailto:George.vanSchoor@nwu.ac.za)

## ABSTRACT

Although self-sensing is not a new concept and the topic has been researched in the past, it remains a challenge. Self-sensing performance is degraded due to problems such as magnetic cross-coupling, eddy currents, saturation and high losses, to name but a few. In this paper the amplitude modulation self-sensing approach using the switching amplifier ripple as high frequency source is adopted. A coupled reluctance network model (RNM) is developed which models the coil impedance at the switching frequency. The model is refined, to accurately include the mentioned degrading effects, and incorporated into a multiple input multiple output (MIMO) parameter estimation self-sensing scheme.

Simulation results show that it is possible to address saturation and magnetic cross-coupling with the RNM incorporated into a MIMO parameter estimation scheme. System sensitivity levels satisfactory for long term operation are achieved.

## INTRODUCTION

In the ongoing drive for wider acceptance and application of active magnetic bearing (AMB) technology in industry, AMB vendors and researchers are striving to make AMBs more reliable and economical. Component integration impacts both cost and reliability and one area of research addressing this issue is self-sensing.

Self-sensing is the concept where the actuation and sensing functions are realised with a single electromagnetic transducer. In the magnetic bearing the coil current and voltage waveforms are monitored and used to extract the rotor position information.

The self-sensing approach adopted by the present work is based on the amplitude modulation approach utilising the switching amplifier ripple as high frequency source. The decision of the amplitude modulation approach is based on the findings of recent experiments and work [1], [2], [3] which establishes that the use of switching ripple for self-sensing leads to

increased robustness above best achievable levels as predicted by [4].

Problems associated with self-sensing include: current ripple amplitude, eddy currents, magnetic material saturation [5] and magnetic cross-coupling [6]. These problems have the potential to degrade self-sensing performance and in some cases even destabilise the self-sensing system.

The problem of current ripple amplitude and the resulting eddy currents seems to be unavoidable for robust self-sensing systems [5]. Solutions to the saturation and cross-coupling problems have however been proposed in literature. Noh [7] proposed a multiple input multiple output (MIMO) parameter estimator approach to overcome problems associated with saturation and Skricka [6] proposed the use of a coupled reluctance network model (RNM) to eliminate the effects of cross-coupling. The present work makes use of these two proposals and implements a frequency shifted model, as proposed by Schammas [1], to reduce the computational cost of the self-sensing scheme. A novel first approach to split the estimation of the two axes while using a single coupled RNM is also presented.

## MODELLING

A prerequisite for self-sensing is that the actuator can be modelled. The scope and accuracy of this model has a direct impact on the self-sensing performance. This section highlights some of the features of the RNM used in the proposed self-sensing scheme. The RNM models the fundamental (switching) frequency impedance of the 8-pole heteropolar magnetic bearing with geometry as shown in Figure 1.

The RNM that is used in the present work is based on [6] and [8]. Figure 2 displays part of the mutual leakage reluctance network that was adopted. The choice of the leakage path was verified with a FEM analysis.

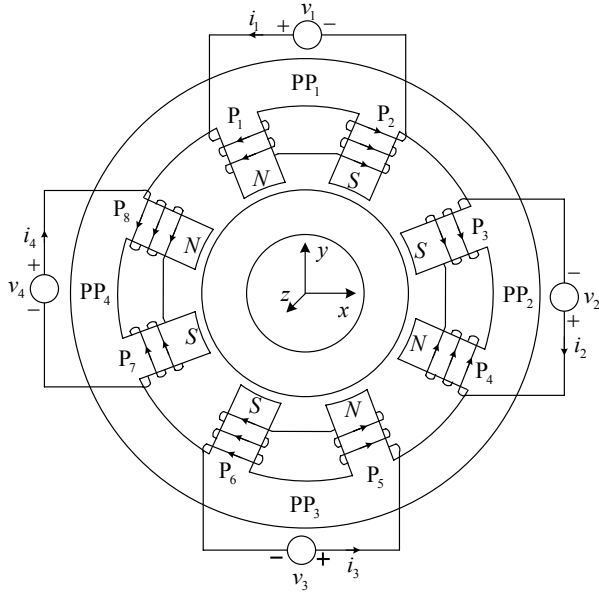


FIGURE 1: 8-pole heteropolar AMB

### Governing equations

A set of  $5P$  linear independent equations linking the  $5P$  fluxes in the AMB is derived in the same fashion as in [6], with  $P$  the number of poles. These equations can be expressed in matrix form as:

$$\mathfrak{R}\Phi = \mathbf{N}\mathbf{I} \quad (1)$$

with  $\mathfrak{R}$  the reluctance matrix,  $\Phi$  the flux vector,  $\mathbf{N}$  the winding matrix and  $\mathbf{I}$  the current vector. The flux in each leg of the RNM can now be determined by inverting the reluctance matrix  $\mathfrak{R}$  as shown in (2).

$$\Phi = \mathfrak{R}^{-1}\mathbf{N}\mathbf{I} \quad (2)$$

The inductance can then be determined from the fluxes utilising [8]:

$$\mathbf{L} = \mathbf{T}'\mathfrak{R}^{-1}\mathbf{N}\mathbf{I} \quad (3)$$

where  $\mathbf{T}$  is defined as a matrix with  $5P$  rows and  $m$  (the number of coils) columns. The  $(k, l)$  entry of  $\mathbf{T}$  represents the number of turns of the  $l^{\text{th}}$  coil about the  $k^{\text{th}}$  flux and should also include the sign according to the chosen convention. In (3) the diagonal entries represent the self-inductances of the coils and the off-diagonal entries the mutual inductances.

### Reluctances

The variables  $\mathfrak{R}_p$ ,  $\mathfrak{R}_r$ , and  $\mathfrak{R}_s$  in Figure 2 correspond to the magnetic iron reluctance of the pole, rotor and stator respectively. These reluctances can be determined using (4).

$$\mathfrak{R} = \frac{l}{\mu_0\mu_r a} \quad (4)$$

with  $l$  the effective magnetic material path length.  $\mu_0$  the permeability of free space,  $\mu_r$  the magnetic material relative permeability and  $a$  the air gap area.

For the present work a frequency shifted model is needed which implies that the RNM must represent the

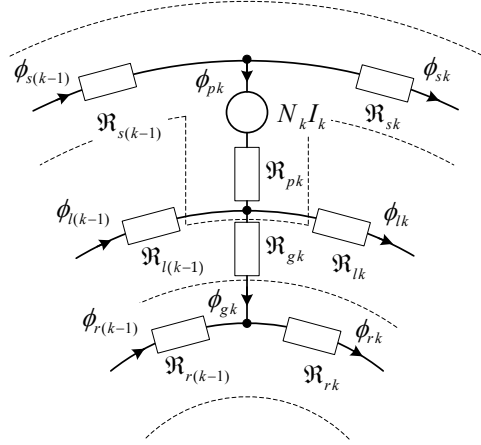


FIGURE 2: Mutual leakage reluctance network

bearing impedance at the switching frequency. To obtain accurate inductance values from (3) the reluctance matrix  $\mathfrak{R}$  has to take the following effects into account:

- eddy currents,
- air gap fringing,
- magnetic material nonlinearity.

The leakage reluctance, which is a constant, is difficult to determine analytically. The reason for this is that the reluctance model is only an approximation of the physical system. The leakage reluctance was therefore determined using MATLAB<sup>®</sup>'s Genetic Algorithm Optimisation Toolbox. The genetic algorithm optimised the leakage reluctance with a cost function that compared RNM results with FEM results. More details regarding this process are discussed in [9].

### Eddy current modelling

The magnetic material is the main contributor to the frequency dependency of the magnetic bearing impedance. The coil current ripple due to switching and the consequent flux ripple causes eddy currents in the magnetic material. Firstly, eddy currents cause ohmic losses which must be drawn from the supply, and secondly eddy currents reduce the flux carrying capacity of the core. For an outside observer with only access to the terminals of the winding this appears as an apparent increase in resistance and decrease in inductance of the equivalent series  $R$ - $L$  circuit. This effect can be modelled in different ways. The approach adopted in the present work is to use a rate dependent material permeability term as presented in [8]:

$$\mu_{fd}(s) = \mu \left[ \frac{\tanh\left(\sqrt{s\sigma\mu} \frac{d}{2}\right)}{\sqrt{s\sigma\mu} \frac{d}{2}} \right] \quad (5)$$

where  $d$  is the lamination thickness,  $\sigma$  is the electrical conductivity,  $\mu = \mu_0\mu_r$  is the material permeability and  $s$  is the complex frequency.

The correlation between the switching frequency impedance of the RNM, as determined using (5) in (3), and the experimental measurements was poor and insufficient for self-sensing implementation. In order to improve the correlation, considerable effort was made to accurately characterise the  $BH$ -curve of the silicon iron laminations. This however did not improve the correlation. The discrepancies are caused by uncertainties regarding the incremental relative permeability  $\mu_{r,\Delta}$  as well as the material resistivity  $\sigma$ .

To overcome this problem the complex material permeability is determined experimentally. This approach resulted in marked improvement in correlation between measured and modelled results.

### Air gap fringing

The air gap reluctance is the parameter that must be estimated, and since it constitutes a large portion of the total reluctance of the magnetic path, the estimated position is sensitive to an error in the air gap model. In [6] the pole face curvature was analysed and the effect of geometric cross-coupling shown. In the present work the effect of fringing is highlighted. When results generated by an analytical air gap model, which excludes fringing, are compared to FEM results, errors as large as 34 % are recorded. Other more complex analytical air gap models may be derived using for instance conformal mapping. For the present work the air gap reluctance is modelled using a lookup table that is generated from FEM results.

### Magnetic material nonlinearity

The nonlinear behaviour of the magnetic material is incorporated into the model by utilising a flux density dependent relative permeability  $\mu_r(B)$ . The governing equations in matrix form are given by (6).

$$\mathfrak{R}(\Phi)\Phi = \mathbf{N}\mathbf{I} \quad (6)$$

The nonlinear relative permeability curve is obtained from the peak magnetisation curve data supplied by the manufacturers of the silicon steel sheets (Cogent™ M400-50A). This information is incorporated into the RNM by using a lookup table.

Figure 3 displays the flow diagram for the nonlinear RNM. As inputs the model receives the rotor position  $(x, y)$  and average coil currents  $(I_1$  to  $I_4)$ . It then uses the  $x$  and  $y$  coordinates to obtain accurate air gap reluctance values for each air gap from a lookup table. The air gap reluctances together with the average coil currents  $I_1$  to  $I_4$  are then used to obtain the fluxes in each leg of the RNM with initial material reluctance values. The new flux levels are then used to determine new material permeability  $(\mu_{0,\mu_r})$  values for each branch of the RNM and a process of iteration is followed until the model converges.

Once the problem has converged the flux levels are used to determine the complex material permeability  $(\mu_{jd})$  for each leg of the RNM from a lookup table. The

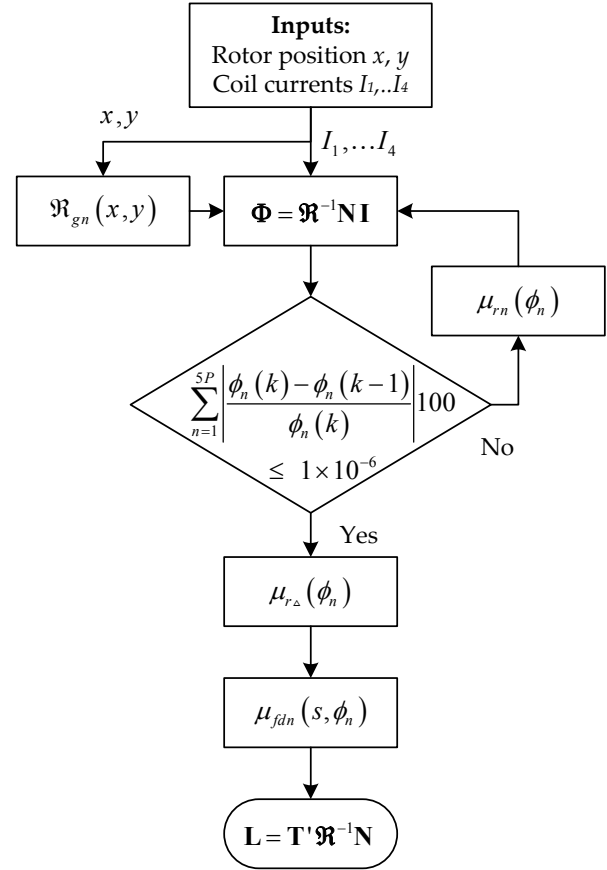


FIGURE 3: Nonlinear RNM flow diagram

complex inductance matrix is then determined from (3) and can be used to determine the complex impedance with  $\mathbf{Z} = j\omega_s\mathbf{L}$  where  $\omega_s$  is the switching frequency.

### Model verification

The first step in the verification process of the RNM is to compare it to a FEM model. Table 1 contains a summary of the maximum absolute percentage errors between the RNM and FEM results for both the linear and nonlinear cases. The linear results of the FEM and RNM correlate closely except for fluxes  $\phi_5$  and  $\phi_6$  which may be attributed to the method employed to determine the flux levels in the FEM model. Discrepancies between the FEM and RNM results for fluxes  $\phi_5$  and  $\phi_6$  are also noticed in the nonlinear analysis for all levels of excitation. The mutual inductance  $L_{13}$  shows good correlation between the FEM and RNM results for the linear case as well as the nonlinear case with low levels of excitation. This further corroborates the claim that the discrepancies in  $\phi_5$  and  $\phi_6$  are due to a measurement error and not due to a modelling error. The results in Table 1 demonstrate the 40 node RNM's ability to achieve high levels of accuracy when compared to an 80,000 node FEM analysis.

**TABLE 1:** Summary of the modelling errors between the FEM and RNM results

Parameter	Maximum absolute error [%]			
	Linear	$I_1 = 2$ A	$I_1 = 6$ A	$I_1 = 10$ A
$L_{11}$	0.95	1.6	1.8	1.5
$\phi_1$	0.85	0.8	0.3	2.3
$\phi_2$	0.85	0.4	0.2	2
$L_{12}$	3.5	4.8	3.8	47
$\phi_3$	11	3.5	8.8	48
$\phi_4$	8	5	7.2	70
$L_{13}$	1.4	2	13.5	73
$\phi_5$	60	10	25	55
$\phi_6$	60	55	90	135
$L_{14}$	3.5	3	4.6	55
$\phi_7$	8	18	35	47
$\phi_8$	11	13	20	44

Experimental results for the magnetic bearing coil impedance at the switching frequency are obtained by exciting the coil of pole pair 1 (PP<sub>1</sub>) with a two-state switching power amplifier (PA). The resulting coil current and voltage waveforms are captured using a digital oscilloscope. The impedance is determined by performing a fast Fourier transform (FFT) analysis on the data and dividing the resulting fundamental voltage component by the corresponding current component. Table 2 contains a summary of the absolute percentage errors between the modelled and measured results and clearly highlights the improvement due to the experimentally determined complex permeability.

### POSITION ESTIMATION

Figure 4 displays the position estimation scheme as implemented in simulation. A transient simulation model (TSM) is used to evaluate the position estimation scheme. The TSM is developed in [10] and accurately models saturation, hysteresis, eddy currents and cross-coupling effects. The amplitude and phase information of the first harmonic components of the magnetic bearing current and voltage waveforms are extracted. The average coil currents are used to determine the flux distribution in the RNM which models the nonlinear behaviour of the magnetic material. The inductance

**TABLE 2:** Summary of the modelling errors between the FFT and RNM results

$I_1$	$ Z_{11} $	$R_{e11}$	$L_{11}$
Datasheet $\mu_r$ and $\mu_{r\Delta}$			
0 A	20 %	42 %	33 %
9 A	60 %	58 %	70 %
Datasheet $\mu_r$ and experimental $\mu_{fd}$			
0 A	13 %	17 %	17 %
9 A	22 %	23 %	22 %

matrix is then used to determine the switching frequency impedance.

The complex voltages are used together with the complex impedance to obtain estimates of the complex coil currents. The errors between the measured and modelled currents are fed to PI controllers which yield estimates of the  $x$  and  $y$  rotor positions. For the self-sensing scheme proposed by the present work the  $x$  and  $y$  estimations are decoupled. The self-sensing scheme is analysed and evaluated in simulation to demonstrate feasibility.

In order to simplify the analysis of the parameter estimator, the coupled network is ignored and each pole pair is treated as an isolated actuator. The simplified actuator can then be represented as shown in Figure 5. The relationship between the voltage, current and position is given by [5]:

$$v = \mu_0 N^2 a \left[ \frac{1}{2(g_0 - x) + \frac{l}{\mu_r}} \frac{di}{dt} + 2 \frac{i}{\left(2(g_0 - x) + \frac{l}{\mu_r}\right)^2} \frac{dx}{dt} \right] + iR \quad (7)$$

with  $N$  the number of coil turns,  $i$  the coil current,  $R$  the coil resistance,  $g_0$  the nominal air gap length and  $x$  the position of the suspended body. Equation (7) assumes uniform distribution of flux throughout the magnetic material and the air gap and neglects leakage, fringing and eddy current effects. In the present work the rotor position can be assumed constant at the switching

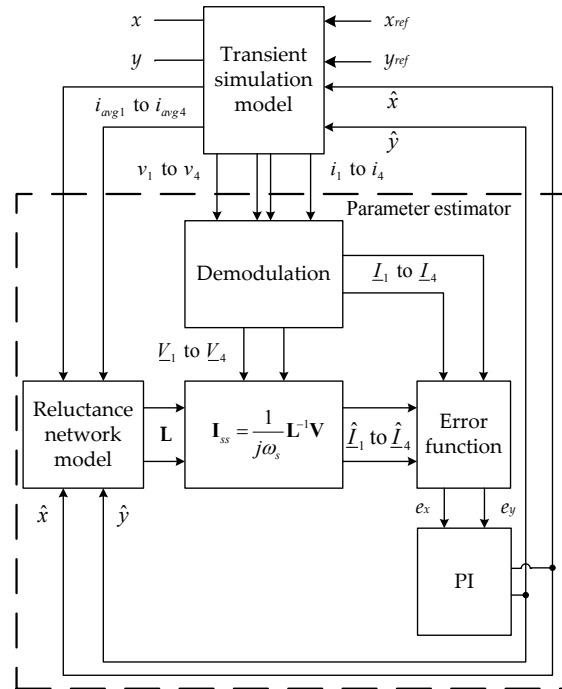


**FIGURE 4:** Position estimation scheme

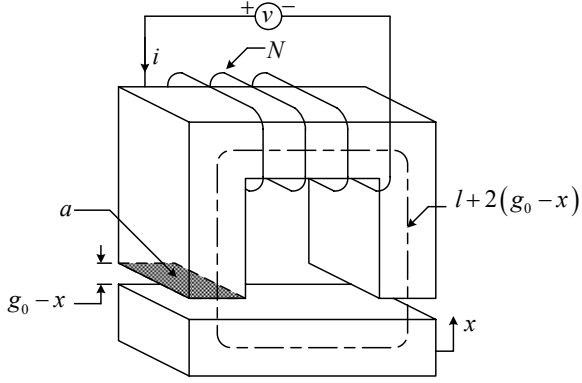


FIGURE 5: Simplified AMB actuator

frequency and the  $dx/dt$  term in (7) may be ignored. Applying the Laplace transform to (7) and expressing it in phasor form at the switching frequency  $\omega_s$ , results in:

$$\underline{V} = \mu_0 N^2 a \frac{1}{2(g_0 \pm x) + l/\mu_r} (j\omega_s) \underline{I} + \underline{I}R \quad (8)$$

Since the coil resistance is small compared to the coil reactance at the switching frequency it may be ignored. Assuming that the amplitude and phase extraction is ideal and neglecting core reluctance, an estimate of the demodulated current is given by:

$$\hat{\underline{I}} = \frac{1}{j\omega_s} \frac{2(g_0 \pm \hat{x})}{\mu_0 N^2 a} \underline{V} \quad (9)$$

As a first approach only the amplitude of the demodulated current estimate is compared to the actual demodulated current amplitude and the error used to update the position estimate  $\hat{x}$ . Mathematically this is represented by:

$$x^* = \arg \min_{\hat{x}} \left( \left| \underline{I} \right| - \left| \hat{\underline{I}}(\hat{x}) \right| \right) \quad (10)$$

with  $\hat{x} \in [x_{min}, x_{max}]$

where  $x_{min}$  and  $x_{max}$  are determined by the backup bearing clearance. The position estimation updates the air gap length which is a parameter of the system, hence the name: parameter estimation.

The simplified structure of the estimator for a single degree of freedom is shown in Figure 6. In the present work coils are configured in differential mode<sup>1</sup> and the geometrically opposing air gaps are given by  $(g_0 - x)$  and  $(g_0 + x)$  respectively. Since both air gaps are influenced by the same change in rotor position  $x$ , it is possible to improve the linearity and signal to noise ratio of the estimated position signal by using information from both coil current waveforms.

The demodulated current amplitudes  $|\hat{L}_2|$  and  $|\hat{L}_4|$ , from the two opposing actuators, are subtracted from each other which eliminates  $g_0$  and results in a signal

that may be used as position error. Unfortunately the signal is not only a function of rotor position but also duty cycle and magnetic saturation. Therefore the voltage signals are demodulated and fed to a frequency shifted model which yields demodulated current amplitude estimates  $|\hat{L}_2|$  and  $|\hat{L}_4|$ . Again the two demodulated current amplitude estimates are subtracted from each other. The estimated displacement signal  $\hat{u}$  is then subtracted from the true displacement signal  $u$  to produce an error  $e$ . The error serves as input to the PI controller which in turn generates the position estimate  $\hat{x}$  that is used in the frequency shifted model. The position estimate is adjusted until the difference in true and estimated demodulated coil currents are identical. The accuracy of the position estimate is therefore a function of the accuracy of the model. The working point dependency of the model is included by feeding the average currents  $i_{avg2}$  and  $i_{avg4}$  to the respective models. In Figure 6  $\lambda_x$  and  $\lambda_y$  are saturation parameters which will be discussed in the results section.

## RESULTS

### Cross-coupling

The effect of coupling between the  $x$ - and  $y$ -axis is investigated by suspending the rotor with the estimated positions and applying a disturbance force in the  $x$ -axis. The saturation parameters  $\lambda_x$  and  $\lambda_y$  are made zero for this investigation. The system is suspended for 50 ms before the sinusoidal disturbance force with an amplitude of 50 N and a frequency of 20 Hz is applied. The mutual inductance terms which interconnect the different pole pairs are initially neglected in the RNM. The system becomes unstable as soon as the disturbance

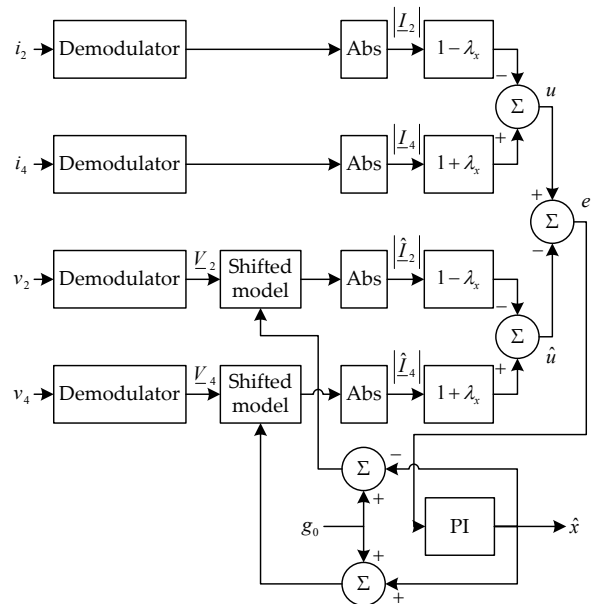


FIGURE 6: Estimator schematic for a single degree of freedom ( $x$ -axis)

<sup>1</sup> Two geometrically opposing actuators are driven symmetrically about some bias point.

force is applied and the rotor de-levitates in the  $x$ -axis. Figure 7 displays the results for the case where the mutual inductance terms are included in the analysis. The inclusion of the mutual inductance terms allows the self-sensing system to stably suspend the rotor in the  $x$ -axis and marked improvement is noted in the  $y$ -axis results. The maximum deviation in the  $y$ -axis error is almost negligible demonstrating the effectiveness of the coupled network model. Ignoring the  $10\ \mu\text{m}$  offset in the  $x$ -axis position, the error amplitude is roughly  $15\ \mu\text{m}$ .

Work done in [6] showed that cross-coupling may not be neglected for certain systems. In the present work it was also shown that cross-coupling may introduce large errors in the estimated position when excluded from the self-sensing model and may even destabilise the position estimation scheme under certain conditions. In [11] the effects of cross-coupling are eliminated by mechanically separating the individual actuators. This approach however has the disadvantage of increasing the manufacturing cost of the magnetic bearing. The present work demonstrates that a coupled RNM may be used in a parameter estimator approach to successfully counteract cross-coupling effects. If it is possible to practically realise the present self-sensing scheme the problem of cross-coupling may be eliminated without mechanical separation of the individual actuators.

### Saturation

Magnetic saturation is perhaps one of the most vexing problems faced by self-sensing researchers today [5]. In order to investigate and quantify the effect of saturation on the performance of the proposed position estimation scheme, the magnetic bearing is intentionally driven into saturation and the estimated position monitored. This is accomplished by pinning the rotor in the zero  $x$ ,  $y$  position, and using the following current references:  $i_{1ref} = i_{3ref} = 7.5\ \text{A}$ ,  $i_{2ref} = 7.5 + 7.5 \sin(2\pi 10t)$  and  $i_{4ref} = 7.5 - 7.5 \sin(2\pi 10t)$ . This leads to magnetic flux densities of above  $1.3\ \text{T}$ .

When one of the opposing pole pairs are driven into saturation, sign reversal takes place which establishes positive feedback and causes the estimated position to clamp at the backup bearing limit. The explanation for this phenomenon is that as the electromagnet saturates, its inductance decreases, resulting in an increase in current ripple. This causes the demodulated current signal of the saturated electromagnet to be more dominant in the position estimation scheme.

Considering only the saturated actuator's response, it is clear where the positive feedback originates from. As soon as the slope of the inductance as a function of position reverses due to saturation, a sign reversal takes place. A solution to this problem is presented in the present work by introducing weights which scale both the transient simulation model (TSM) and RNM demodulated currents. The weights are adjusted to

ensure that the actuator with the lowest flux density contributes the most to the position estimate. This approach is graphically presented in Figure 6 where the saturation factor  $\lambda_x$  is defined as the difference between the average flux densities of the two opposing pole pairs (PP<sub>2</sub> and PP<sub>4</sub> in Figure 1). The saturation factors  $\lambda_x$  and  $\lambda_y$  are determined from:

$$\lambda_y = \left( (B_1 - B_2) - (B_5 - B_6) \right) / 2 \quad (11)$$

$$\left\{ \lambda_y \in \mathbb{R} \mid -1 \leq \lambda_y \leq 1 \right\}$$

$$\lambda_x = \left( (B_4 - B_3) - (B_8 - B_7) \right) / 2 \quad (12)$$

$$\left\{ \lambda_x \in \mathbb{R} \mid -1 \leq \lambda_x \leq 1 \right\}$$

Parameters  $B_1$  to  $B_8$  are the respective flux densities for poles  $P_1$  to  $P_8$  and the signs in (11) and (12) correspond to the referencing convention used throughout the paper as illustrated in Figure 1. The weighting concept is recommended as opposed to using only the demodulated coil current of the actuator with the lowest flux density. This approach is advantageous for two reasons; firstly to eliminate discontinuities in the estimated position which will occur when switching between the two demodulated currents, and secondly to exploit the advantages of the differential configuration under normal operation namely increased in sensitivity

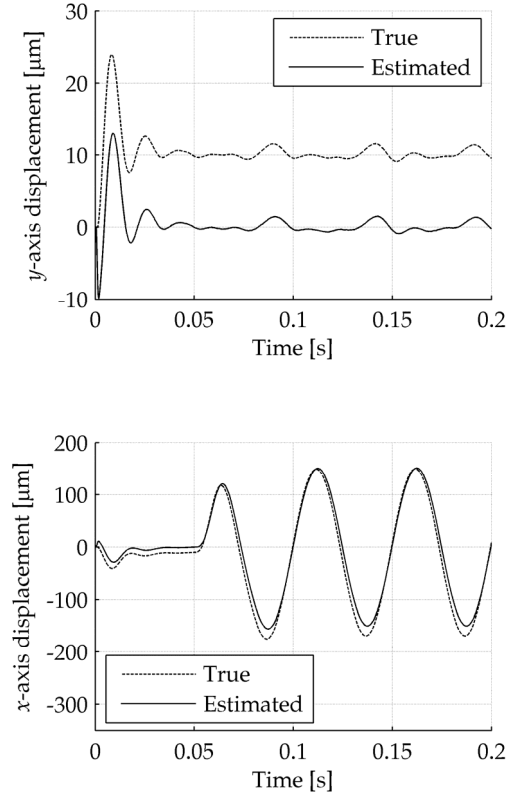


**FIGURE 7:** Dynamic cross-coupling effects (disturbance force of  $50\ \text{N}$  on  $x$ -axis from  $50\ \text{ms}$ , mutual inductances included)

and linearity.

The proposed current weighting scheme is now evaluated under the exact same excitation conditions of the previous result. Figure 8 displays the position estimation results. As is evident from the  $x$ -axis results the estimated position deviates less than  $5\ \mu\text{m}$  from the dc offset of  $\pm 12\ \mu\text{m}$  for flux densities peaking at over 1.3 T. This is a remarkable result indicating that the proposed self-sensing scheme may eliminate the problems posed by saturation when only one of the two opposing electromagnets is driven into saturation.

### Bandwidth

The frequency response of the estimated position compared to the true position is analysed by adding a constant amplitude sinusoidal signal to the position reference signal. Small position and current variations are used so that the system may be assumed linear in the working point. The frequency of the reference signal is increased from 10 Hz up to 2 kHz which is well above the expected self-sensing bandwidth.

Figure 9 displays the frequency response of the estimated position compared to the true position as determined from simulation. The point where the estimated and true positions deviate more than 3 dB is reached at 270 Hz. The self-sensing bandwidth may however be lower than 270 Hz since the phase lag at this point is already 40 degrees. The bandwidth of the position estimation scheme is very low which has an undesirable effect as will be demonstrated in the following section.

### Stability margin

The stability margin for the system or system sensitivity is determined according to ISO 14839-3. The system sensitivity curve for position control with the true position yields a peak sensitivity of 4 dB. Figure 10 displays the sensitivity curve with position control implemented with the estimated position. A peak sensitivity of 8 dB is recorded. This implies that the performance is satisfactory for unrestricted long-term operation.

The focus of the present work was however not to implement an optimum parameter estimator scheme which utilises the RNM to accomplish self-sensing, but to merely demonstrate the feasibility. Further work is therefore needed to optimise the position estimation scheme in order to achieve better system robustness. Issues that may be looked at include the demodulation process that was used and the use of both the amplitude and phase values of the demodulated currents as input to the parameter estimator. A more elaborate parameter estimation scheme may also be investigated where the  $x$ - and  $y$ -axis are not decoupled.

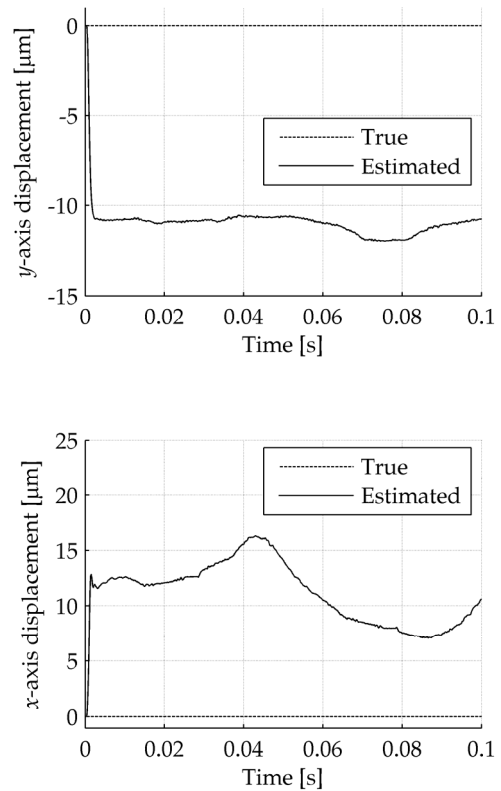


FIGURE 8: Effect of magnetic saturation on position estimation (current weighting included)

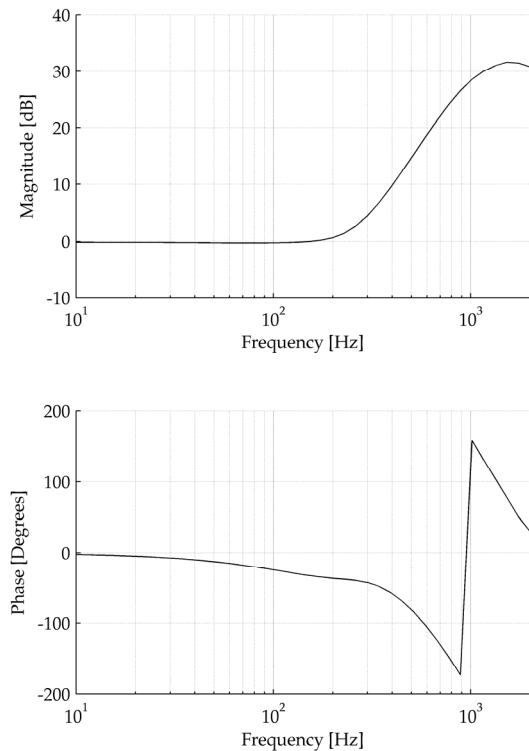
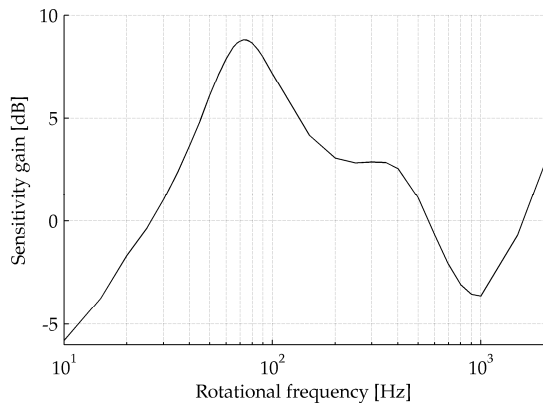


FIGURE 9: Frequency response of the estimated position with respect to the true position



**FIGURE 10:** Bode plot of the sensitivity function  $G_s$  (suspension with estimated position)

## CONCLUSION

The present work demonstrates the possibility of constructing a MIMO parameter estimation self-sensing scheme, with a coupled RNM at the heart, that alleviates problems such as saturation and cross-coupling. This was however only a first approach to demonstrate the suitability of the refined RNM for such a scheme and future work is needed to analyse and optimise the MIMO parameter estimation scheme.

The self-sensing scheme proposed in the paper is difficult to stabilise and displayed inferior levels of sensitivity and bandwidth compared to dedicated position sensors. The estimation of the  $x$  and  $y$  rotor positions is accomplished with two separate parameter estimators and one coupled RNM. In a thorough analysis a state space model of the AMB system can be developed, which will then facilitate the robustness analysis of the proposed MIMO self-sensing scheme with established methodologies e.g.  $\mu$ -analysis to optimise estimator performance.

There are two commercial applications of the self-sensing technology to date and both place moderate requirements on the position estimation [5]. Much work is still needed to realise a self-sensing scheme that will meet more stringent requirements. Self-sensing therefore remains a tough challenge with several unaddressed issues.

## REFERENCES

- [1] A. Schammas, "A self-sensing active magnetic bearing: Modulation approach," PhD thesis, Swiss Federal Institute of Technology Lausanne - EPFL, Lausanne, Switzerland, July 2003.
- [2] D. T. Montie, "Performance limitations and self-sensing magnetic bearings," PhD Thesis, University of Virginia, Virginia, USA, Jan. 2003.
- [3] E. H. Maslen, D. T. Montie, and T. Iwasaki, "Robustness limitations in self-sensing magnetic bearings," ASME Journal of Dynamic Systems,

Measurement and Control, vol. 128, pp. 197–203, Jun. 2006.

- [4] N. Morse, R. Smith, B. Paden, and J. Antaki, "Position sensed and self-sensing magnetic bearing configurations and associated robustness limitations," in Proceedings of the 37th IEEE Conference on Decision and Control, vol. 3, Tampa, Florida USA, Dec. 1998, pp. 2599–2604.
- [5] E. H. Maslen, "Self-sensing for active magnetic bearings: overview and status," in Proceedings of the 10th International Symposium on Magnetic Bearings, Martigny, Switzerland, Aug. 2006, pp. 13–19.
- [6] N. Skricka and R. Markert, "Influence of cross-axis sensitivity and coordinate coupling on self-sensing," in Proceedings of the Sixth International Symposium on Magnetic Suspension Technology, Turin, Italy, Oct. 2001, pp. 179–184.
- [7] M. D. Noh and E. H. Maslen, "Self-sensing magnetic bearings (Part II)," in Proceedings of the Fifth International Symposium on Magnetic Bearings, Kanazawa, Japan, Aug. 1996, pp. 113–118.
- [8] D. C. Meeker, E. H. Maslen, and M. D. Noh, "An augmented circuit model for magnetic bearings including eddy currents, fringing, and leakage," IEEE Transactions on Magnetics, vol. 32, no. 4, pp. 3219–3227, July 1996.
- [9] E.O. Ranft, "An improved model for self-sensing heteropolar active magnetic bearings," PhD thesis, North-West University, Potchefstroom Campus, South Africa, February 2008.
- [10] M. D. Noh, D. T. Montie, and E. H. Maslen, "A simulation model for the analysis of transient magnetic bearing performance," in Proceedings of the 7th International Symposium on Magnetic Bearings, ETH Zurich, Switzerland, Aug. 2000, pp. 177–181.
- [11] A. Schammas, R. Herzog, P. Bühler, and H. Bleuler, "New results for self-sensing active magnetic bearings using modulation approach," IEEE Transactions on Control Systems Technology, vol. 13, no. 4, pp. 509–516, Jul. 2005.